

Microstructural investigation of an extruded austenitic oxide dispersion strengthened steel containing a carbon-containing process control agent

Tim Gräning^{*a}, Michael Rieth^a, Jan Hoffmann^a, Sascha Seils^{a,b}, Philip D. Edmondson^c, Anton Möslang^a

- a) Institute for Applied Materials (IAM), Karlsruhe Institute of Technology (KIT), Hermann-von-Helmholtz-Platz 1, 76344 Eggenstein-Leopoldshafen, Germany
- b) Karlsruhe Nano Micro Facility (KNMF), Karlsruhe Institute of Technology (KIT), Hermann-von-Helmholtz-Platz 1, 76344 Eggenstein-Leopoldshafen, Germany
- c) Materials Science and Technology Division, Oak Ridge National Laboratory, Oak Ridge, TN 37831, USA

*Corresponding author. Tel +49 721 608 24093; fax: +49 721 608 24567. tim.graening@kit.edu
E-mail address: michael.rieth@kit.edu; j.hoffmann@kit.edu; sascha.seils@kit.edu; edmondsonpd@ornl.gov; anton.moeslang@kit.edu

Abstract

The adhesion of austenitic oxide dispersion strengthened (ODS) steel during mechanical alloying and a decreased powder production yield can be overcome by the addition of a process control agent: stearic acid. Here, the influence of stearic acid and the introduction of carbon in an extruded and annealed austenitic ODS steel was investigated. In particular the impact of carbon on the precipitate formation, the stability of particle and grain sizes during a heat treatment of 2 h at temperatures in a range between 500 and 1100 °C and the resulting grain size were investigated. No direct influence of carbon on the formation of precipitates was detected in the as-extruded condition. The orientation relationship of oxide nanoparticles and the austenitic matrix was found to be size dependent. Also, a surprising growth of oxide precipitates was recorded, which starts at annealing temperatures as low as 700 °C. Precipitates in other steels do not show a growth in this temperature regime at all. For that reason, a possible link between the unexpected growth and the formation of carbides was investigated. M_7C_3 and $M_{23}C_6$ carbides were found in every sample condition and we were able to show that their amount follows a trend suggested by thermodynamic simulations. The grain size of the extruded austenitic ODS steel was examined and a grain refinement was found after a heat treatment of 2 h at 700 °C or higher was performed. That is caused by the inhibition of further grain growth after nucleation as part of the recrystallization process has happened. The dragging force exerted by precipitates is strong enough to pin grain boundaries. Nevertheless, no direct impact of carbon on the oxide precipitate growth was found, an indirect impact of carbon on the growth of ODS precipitates is supposed but requires long-term annealing studies to be verified.

Keywords:

- Austenitic steel
- ODS
- Process control agent
- Mechanical alloying
- TEM
- APT
- EBSD

1. Introduction

The successful introduction of nano-particles in ferritic steels achieved enhanced high-temperature properties and radiation resistance, but this was accompanied by a reduced ductility and partial embrittlement of these so-called 'oxide dispersion strengthened' (ODS) steels [1, 2]. For this reason, interest in introducing nano-precipitates during the more ductile, austenitic phase has grown stronger and can be seen in the growing number of publications in this research area since 2008 [3]. Like their ferritic counterpart, the austenitic ODS steels are designed to be used as a structural material in future fusion power plants and, therefore, the majority of the research was targeting the development of a material with superior strength and ductility in comparison to ferritic ODS steels at high temperatures [4–9]. However, only few publications have discussed the decreased powder yield of austenitic ODS steels produced via mechanical alloying [10–12]. Due to the increased adhesion of the ductile, austenitic powder on the walls of the milling vessel, it is necessary to add a process control agent (PCA) to the powder to achieve a production yield of 100 % [10–12]. The adhesion of ductile powders during mechanical alloying is a well-known problem, which was already reported for aluminum and was tackled by the addition of a carbon-rich PCA [13, 14]. Applying this method to the processing of austenitic ODS steels helped to overcome this drawback by coating the surface of the powder particles during the mechanical alloying process, but it has yet to be shown how this affects the microstructure and the mechanical properties of the final product.

Here we investigate the possible influence of a carbon-rich PCA on the formation of ODS precipitates in extruded rods and evaluates the changes during a short-term annealing of two hours at different temperatures using transmission electron microscopy (TEM) and atom probe tomography (APT) methods. To shed light on the impact of carbon, not only on the precipitates but also on the grain size, scanning electron microscopy (SEM) and electron backscattering diffraction (EBSD) methods were applied. The findings were compared to thermodynamic simulations.

2. Materials and Methods

2.1. Materials

The material was produced using a novel two-step mechanical alloying process using a steel prealloy, Fe_3Y , elemental nickel powder and stearic acid as a PCA. In house investigations have shown that Fe_3Y is easier to dissolve and distribute than the more commonly used Y_2O_3 and helps to reduce the milling time. The first and second milling step were performed in batch sizes of 200 g and have taken 20 and 12 h, respectively. The whole process is described elsewhere in more detail [12, 15]. After mechanical alloying, the powder was used to fill a stainless steel can of 80 mm diameter and 100 mm in height. The steel can was degassed at 450 °C under an applied vacuum of 2×10^{-5} mbar and then sealed. It was directly extruded at a temperature of 1100 °C (in one-step) to form a rod 15 mm in diameter corresponded to a deformation degree of -1.67. The actual chemical composition of the extruded rod is listed in Table 1 and labeled as PCA-2 for consistency with the mentioned prequel. A triple determination method was used for each analyzing method and all powders. The carrier gas hot extraction method was applied to determine the amount of oxygen, while carbon was measured using a carbon/sulfur analyzer. All other elements were identified after they were dissolved in a mixed acid using inductively coupled plasma optical emission spectrometry (ICP-OES). Parts of the approximately 2 m long rod were then heat-treated for 2 h at 500, 700, 900 or 1100 °C to determine the influence of a subsequent annealing on the evolution of the ODS precipitates and the microstructure.

It was also demonstrated in a previous publication, that the milling process was successful with the addition of a carbon-containing process control agent (PCA) and that a powder production yield of 100 % can be attained [15]. Here, the impact of carbon is analyzed in extruded rods. An overview of the microstructure and distribution of carbon and a thorough evaluation of the orientation relationship of particles and the austenitic matrix are shown with respect to the size of the oxide nanoparticles formed. Atom probe tomography methods were applied to investigate changes in the microstructure, such as the growth of precipitates and the change in the number density of precipitates with respect to the chosen annealing temperature.

Table 1 Determined chemical composition of the extruded rod in wt.-%.

Rod	Fe	Cr	Ni	W	Mn	Ti	V	Y	O	C
PCA-2	balance	16.00	14.10	1.52	0.37	0.16	0.16	0.18	0.14	0.28

2.2. Microscopy

Samples for transmission electron microscopy (TEM) were prepared by cutting off thin slices of the extruded rod to a thickness of approximately 1 mm, followed by grinding and polishing of the slices to achieve a thickness of 0.1 to 0.2 mm. Three small discs with a diameter of 3 mm were punched out of each prepared slice. Finally, electro-polishing in a TENUPO V device with an electrolyte mix of 20% H₂SO₄ and 80% CH₃OH was carried out at 20 °C, followed by a cleaning step applying a precision ion polishing system.

TEM studies were carried out with an FEI Tecnai 20 FEG analytical microscope with an accelerating voltage of 200 kV and a high angle, annular dark field detector. Energy dispersed X-ray spectroscopy (EDS), in combination with scanning TEM (STEM) mode, was recorded using an EDAX Si(Li) detector with an ultra-thin window and a FEI double tilt holder. The recording and determination of diffraction patterns was performed using Digital Micrograph (by GATAN) and ImageJ software [16]. Structural information from the ICSD database gave Y₂TiO₅ (a = 1.0350 nm; orthorhombic), Y₂Ti₂O₇ (a = 1.0095 nm; pyrochlore) and Y₂O₃ (a = 1.0600 nm; bixbyite) as possible phases for nanoclusters and of γ-iron (a = 0.365 nm; Cu structure type) for the austenitic matrix that has been used for evaluation [17–19].

Samples for scanning electron microscopy (SEM) were ground and polished in the same way as the TEM samples but instead of punching three small discs out of the ROI, the whole sample was electro-polished for 15 seconds at 12.5 V using the same electrolyte as for the TEM samples. Finally, the surface was cleaned using isopropanol before investigation of the samples was carried out on a Zeiss Merlin field-emission gun scanning electron microscope, with GEMINI II electron optics and an acceleration voltage of 20 kV for electron back scattering diffraction (EBSD). Kikuchi patterns were recorded with an EDAX Hikari high-speed EBSD camera and evaluated by TEAM and OIM Analysis 7.0 software. A minimum confidence index (CI) of 0.1 was applied, misorientation angles higher than 10° were set as grain boundaries and all typical Σ3 coincidence side lattice (CSL) for a face-centered cubic lattice (60° on the {111} plane) were identified. All maps are presented and evaluated in an orthogonal direction with respect to the sample. A minimum confidence index (CI) of 0.1 was applied, misorientation angles higher than 10_ were set as grain boundaries and all typical Σ3 coincidence side lattice (CSL) for a face-centered cubic lattice (60° on the {111} plane) were identified. Finally as a clean-up step a grain CI standardization with a tolerance angle of 5° was applied to all EBSD maps.

2.3. Atom probe tomography

APT experiments were performed in a LEAP 4000X HR local electrode atom probe, produced by CAMECA Instruments Inc. The specimens were analyzed in laser-mode at a sample temperature of 40 K. A pulse repetition rate of 200 kHz, focused laser beam energy of either 75 or 100 pJ, and a data collection rate between 0.3 % and 1% ions per field evaporation pulse were applied. Between 266 and 370 million atoms were collected for each heat treated condition. Surface regions that contained damage from the gallium ion beam have not been used for the evaluation. Data analysis was performed using the IVAS 3.6.14 software package by CAMECA Instruments Inc. The maximum separation method described elsewhere was used to identify the nanoclusters for further analysis [20]. A value between 8 and 12 was selected as a cut-off limit for the minimum size of a cluster N_{min} and value of 1.0 nm was used as the maximum separation d_{max} of core ions.

The average radii of the yttrium and titanium-rich clusters were calculated by using the spherical equivalent radius (SER) R given by Refs. [21,22]:

$$R = \sqrt{\frac{3N}{4\pi\rho Q}},$$

where N is the number of titanium and yttrium atoms in each precipitate, ρ is the density of the precipitates, and Q is the detection efficiency of the atom probe used, which was taken to be 0.4. For comparison reasons, the calculated radii of precipitates were also determined by applying an often-used method: the Guinier radius R_g . It is given by Ref. [23]:

$$R = \sqrt{\frac{5}{3}}l_g,$$

where l_g is the radius of gyration. The measurements of the diameter were performed parallel to the analysis direction, as proposed in a publication by London et al. [24].

3. Results & Discussion

3.1. Microstructure in the extruded condition

The sizes, distribution and orientation relationship of the precipitates (as well as the grain size of as-extruded material) were investigated to set a baseline for a comparison with the annealed samples. For those investigations, the influence of carbon was discussed and evaluated in each section. To get a general impression of the microstructure, a high-angle annular dark field (HAADF) image of the rod was taken with the normal direction of the presented plane parallel to the extrusion direction and is pictured on the left-hand side of Figure 1. The EDS maps on the right-hand side of Figure 1 show the formation of a large carbide with a diameter of 500 to 700 nm. It is incorporated into the austenitic matrix. The carbide consists of several elements, namely chromium (Cr), vanadium (V), tungsten (W), and manganese (Mn). An enrichment of oxygen and carbon can be seen by comparing the EDS maps of both elements. It can be inferred that the formation of nano-sized oxides and larger, complex carbides occur in conjunction with each other during the extrusion process. After mechanical alloying, no carbide-rich precipitates were found inside the powder particles and this means that their formation and growth occurs during the extrusion process. Several ODS particles were found at and near to the grain boundary of the carbide, which can be seen as a first indication of their restraining force on grain boundary migration. A lot of small ODS precipitates consist of multiple phases clustered next to each other. This phenomena can be observed in the particle in the enlarged area in the top left of the HAADF image in Figure 1 and it has also been reported by other researchers [21]. The two circled regions have a darker contrast and contain elements with a lower atomic number. Comparing this enlarged particle with the element maps on the right-hand side reveals that it contains vanadium (V), titanium (Ti), yttrium (Y), and oxygen (O). Vanadium inside the nano-particles can impede the capillary-driven particle coarsening by reducing the interface energy and this can be a beneficial contribution [22, 23]. A couple of these multi-phase particles with a diameter in the range 15 to 25 nm were found across the whole sample, whereby the majority of the small particles with a diameter less than 10 nm contain high amounts of Y, Ti, and O.

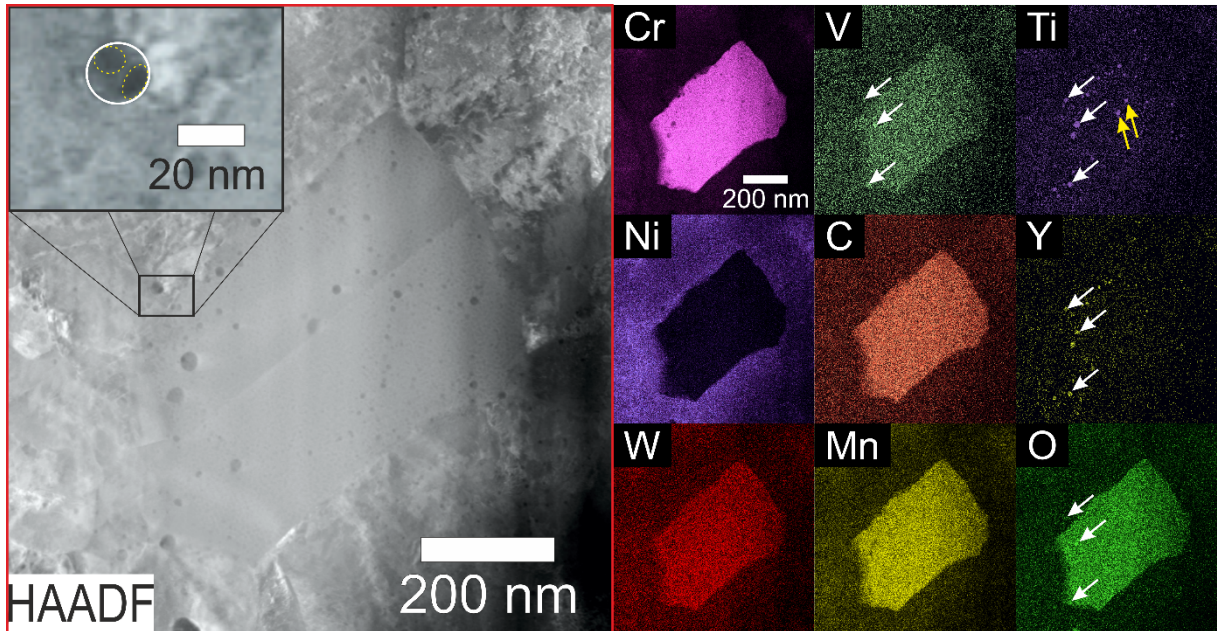
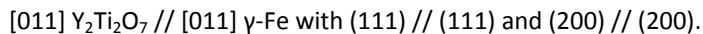


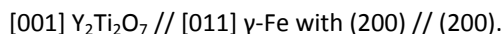
Figure 1 HAADF TEM image of the microstructure of the as-extruded rod next to EDS maps showing the significant elements in the same area. Yellow arrows highlight Ti-O precipitates, while white arrows display complex Y-Ti-V-O particles.

For a basic understanding of the growth behavior of ODS precipitates at elevated temperatures and their influence on mechanical properties, it is important to determine the orientation relationship between the particles and the matrix. Knowing the phase composition and obtaining information about the orientation relationship of particles and matrix enables the calculation of the interface energy, which is an important factor in predicting the growth of precipitates at high temperatures [24]. Thus, high-resolution transmission electron microscopy (HRTEM) images of precipitates with different diameters were taken and are presented in Figure 2. A dashed yellow circle marks a precipitate with a diameter of approximately 10 nm. Next to this larger precipitate, smaller ones were found and some of them are highlighted with blue dashed circles. On the top right of Figure 2, an image of the fast Fourier transformation (FFT) of the entire HAADF image is presented which reveals the reciprocal lattices of several precipitates and the austenitic matrix. On the bottom right, a detailed evaluation of the FFT is depicted, where the yellow box and blue circles represent reflexes produced by the large and several smaller precipitates, respectively. The red colored reflexes are representative of the reciprocal lattice of the austenitic matrix. The precipitates were found to correspond to the $Y_2Ti_2O_7$ phase. It can be seen that the size of the precipitates does have an impact on the orientation relationship. The austenitic matrix and the small precipitates both exhibit a $\{011\}$ zone axis and the orientation relationship can be expressed as follows:



Essentially, this means that a cube-on-cube relationship between particles and matrix exists, which has also been found for ferritic ODS steel [25, 26]. This orientation relationship was also found to be true for austenitic ODS steels by other researchers [27].

In contrast, bigger precipitates tend to have a different orientation relationship with the austenitic matrix, which turns out to be of the following type:



An inverse FFT image displayed in the bottom left image in Figure 2 was generated using the yellow marked reflexes and proves that the reflexes belong to the bigger precipitate. The lattice mismatch δ between the matrix and the particle was calculated using the formula $\delta = |2 \cdot (d_1 - d_2) / (d_1 + d_2)|$ and is displayed in Table 2. The often-reported orientation relationship of the (400) & (200) plane (with a very low mismatch of only 0.3% between $Y_2Ti_2O_7$ and the austenitic matrix) was not found but is listed for comparison reasons [7]. Similar to the results found by Miao et al. [27], most precipitates larger than 15 nm in diameter exhibit an incoherent and

random orientation relationship. Coherent precipitates are twice as effective as incoherent precipitates in pinning boundary migration and can suppress recrystallization more efficiently, due to the higher interface energy in an incoherent precipitate. This extra energy must be spent by the passing boundary to form an incoherent interface [28]. However, all precipitates exert a drag force on a boundary and prevent grain growth to a certain extent, which is known as the Zener pinning. The small radius, high number density, low interface-energy, and rounded shape of the precipitates are beneficial to increasing the Zener drag. For that reason, small coherent precipitates can prevent grain growth at higher temperatures more effectively. The stress field leads to an increased threshold energy, which needs to be overcome by dislocations to continue their motion. This eventually results in an increased yield strength for material with precipitates [28, 29].

In terms of mechanical properties, it is of interest to determine the amount and the size of the formed carbides, which can severely affect the mechanical properties. It is well known, that $M_{23}C_6$ carbides can cause embrittlement and decrease the ductility [30, 31] but the focus of the TEM investigation was to analyze the influence of carbon on the formation of nano-scale oxide precipitates. In extruded material, the impact of carbon on the microstructure was not visible in terms of the precipitate orientation or phase formation. However, one indirect influence resulting from a driving force for the formation of carbides with elements (which are important for the formation of ODS precipitates), was observed in heat-treated powder and needs to be investigated by further methods in extruded material [15].

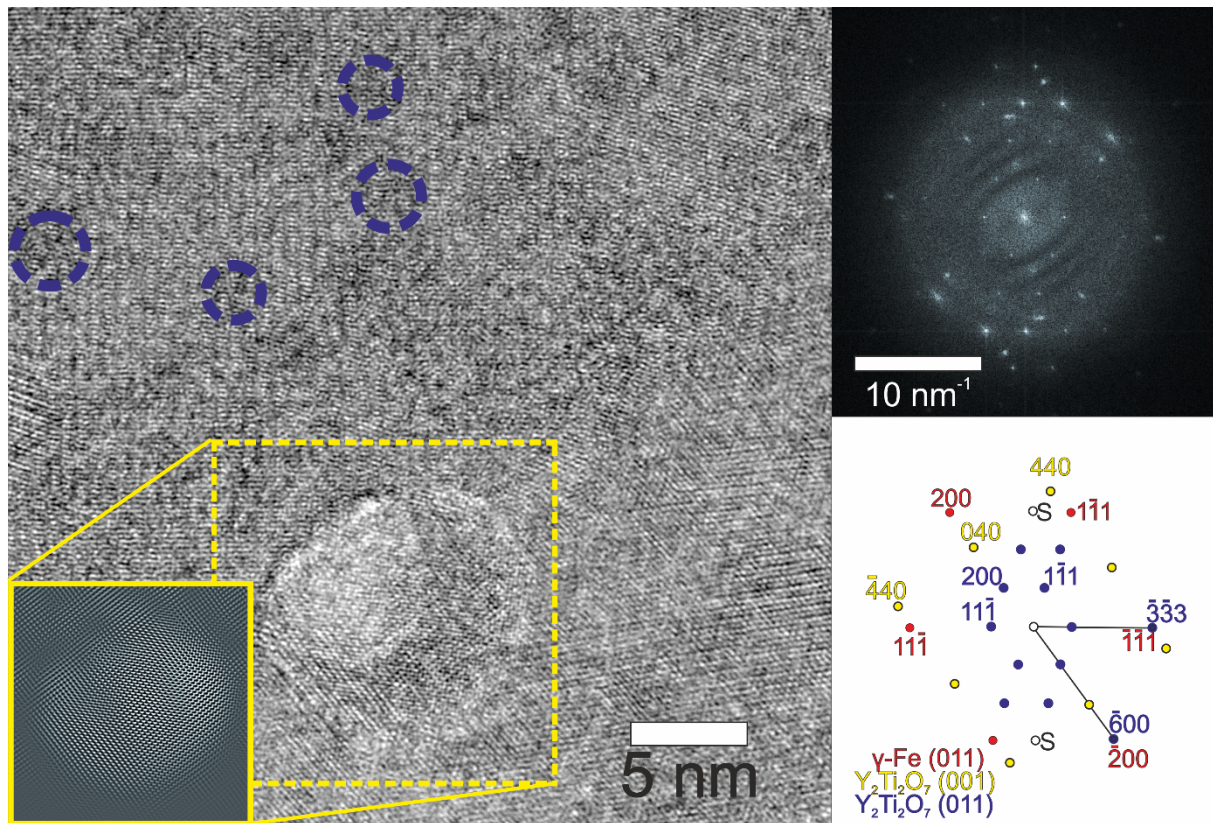


Figure 2 Determination of the orientation relationship between particles and the austenitic matrix in respect to their size in as-extruded condition.

Table 2 Mismatch between selected lattice planes of $Y_2Ti_2O_7$ and austenite.

(hkl)	d (hkl) / nm		Mismatch δ
	$Y_2Ti_2O_7$	Austenite	
$Y_2Ti_2O_7$ & Austenite			
(333) & (111)	0.1943	0.2055	5.6 %
(600) & (200)	0.1683	0.1780	5.6 %
(400) & (200)	0.1785	0.1780	0.3 %
(800) & (220)	0.1262	0.1259	0.3 %

3.2. APT

For additional insights into the three dimensional distribution and the size of the precipitates, APT samples have been investigated. The APT results of the as-extruded material are displayed in Figure 3. A region inside the austenitic matrix was chosen to analyze the nano-particles. Figure 3 shows accumulations of carbon along a grain boundary (GB) in the middle of the tip. This grain boundary separates two grains with vastly different microstructures. The top part of the tip has a much lower number density of precipitates in comparison with the bottom half of the tip. This leads to the conclusion that regions with different number densities of precipitates co-exist next to each other. As a consequence, the determined volume fraction of particles might not be representative for the entire material, due to the limited volume of the specimen tested. However, large differences in the number density of ODS precipitates in other mechanically alloyed ODS steels are often reported [32].

Carbon is one of the elements most likely to form chromium carbides because of its abundance as one of the major elements in the alloy and the low Gibbs energy of chromium carbides [33] but it was not found in the proximity of the oxide-rich precipitates. A thorough examination of the precipitates shows that the APT results are in good agreement with the findings of the TEM EDS analysis and confirm the contribution of vanadium atoms in multiple precipitates. Chromium and iron atoms were also found inside and around the precipitates and can possibly be attributed to flight-path aberrations, due to differences in the evaporation field of oxide particles and the matrix. However, a core-shell structure (often reported for ferritic ODS steels) was not observed [34–37]. Its absence can be explained by the significantly smaller mismatch between the precipitates and the austenitic matrix of only $\delta = 5.6\%$ instead of the reported 12.6 % for the (110)//(440) mismatch in ferrite and a low surface energy of $Y_2Ti_2O_7$ which may make a buffer chromium layer between the precipitates and the matrix redundant [25, 34, 38].

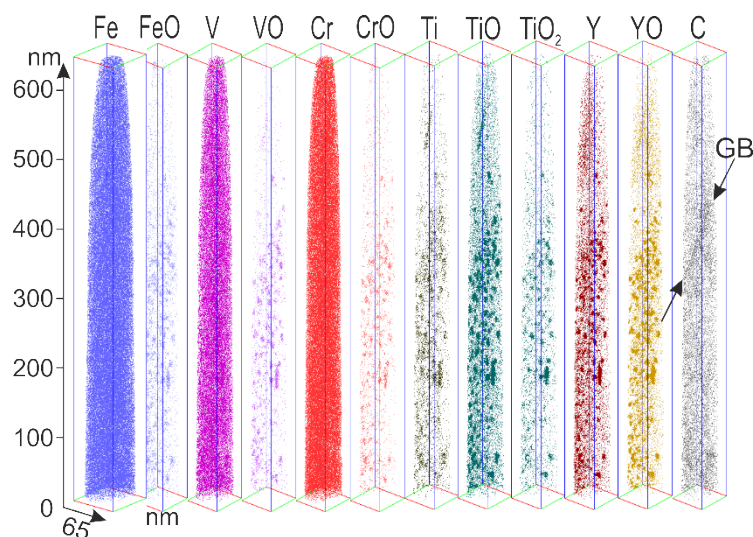


Figure 3 Results of an APT-measurement of PCA-2 in as-extruded condition showing a precipitate-rich area in the middle of the tip and a particle-voided area at the top of the tip.

After setting the baseline with the investigation of the as-extruded material, the annealed material was examined to follow the evolution of the precipitates and to determine a possible impact of carbon. A representative overview of the microstructure of several grains with differently sized precipitates for the material is shown in Figure 4; this was annealed at 1100 °C for 2 h.

A large precipitate containing Ti-V-O, a smaller precipitate mostly comprising Cr-W-Mn-C, several Y-O particles and a few precipitates containing Y-Ti-O were identified. A decreased Cr, W, and Mn content along the grain boundaries is also visible and indicates diffusion of those elements along the grain boundary, to form carbide precipitates [39, 40].

It is also noticeable that argon gas, which was used as an inert gas during mechanical alloying, was found as an impurity adjacent to the small Y-O and Y-Ti-O precipitates. This [41, 42]. That can be explained by a low interface energy between the nano-precipitates and the austenitic matrix, which lets the nano-particles act as sinks for vacancies and argon gas bubbles [7, 43–47]. However, argon bubbles have a negative effect on mechanical properties when they are attached to ODS precipitates. A decreased strengthening effect by the precipitates, caused by a reduced pinning pressure exerted on dislocations, is detectable [48]. Therefore, the amount of argon introduced to the matrix material during mechanical alloying should be minimized. The perfect ratio between yttrium, titanium, and oxygen (in weight percentage) to form the preferred $Y_2Ti_2O_7$ precipitates is 1.00 to 0.54 to 0.86 [12]. The $Y_2Ti_2O_7$ phase is preferred because of its high temperature stability and the low potential for precipitate coarsening, due to its low interface energy in an austenitic matrix [25]. In the case of material PCA-2, and following chemical analysis by ICP-OES, the ratio is 1.00 to 0.89 to 0.78 for the aforementioned elements. Comparison between these values implies that an excess of titanium and a lack of oxygen are present in PCA-2. Larger, unwanted Ti-V-O precipitates have formed due to the abundance of titanium: high titanium content and the low amount of oxygen contribute towards the formation of Ti_2O_3 , Ti-V-O and Y_2O_3 instead of forming $Y_2Ti_2O_7$, due to the lower oxygen-demand required to form Ti_2O_3 and Y_2O_3 . This trend was also observed in annealed powder samples [15].

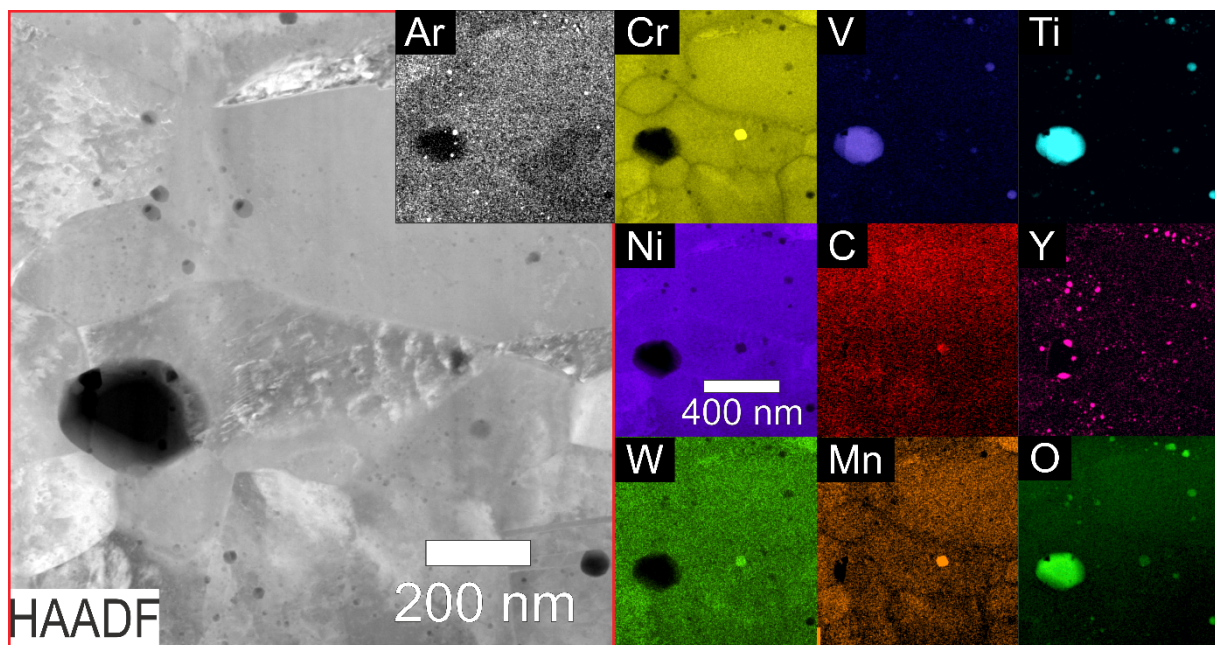


Figure 4 HAADF image of the microstructure after a short-term annealing for 2 h at 1100 °C.

In this context, it is also important to note the size differences of the much larger titanium-rich and smaller yttrium-rich oxides depicted in Figure 4. It is necessary to examine the diffusion coefficients of titanium and yttrium in austenitic steel and to take the differences in the free Gibbs energies of the formed precipitates into consideration. Jiang et al. [43] have done thermodynamic simulations on the formation of ODS precipitates and suggested that yttrium, which was either dissolved or fractured and homogeneously distributed during the

mechanical alloying process, forms Y_2O_3 when there is a low partial pressure of oxygen and a high temperature [43, 49]. In addition, an increased diffusion coefficient of titanium (approximately 7.6 times that in austenitic steel, compared to the ferritic counterpart), is attributed to its high diffusivity [50]. The combination of a low oxygen level, the low free Gibbs energy of Y_2O_3 and Ti_2O_3 , and the high diffusivity of titanium and oxygen in austenite explains the formation of Ti_2O_3 and Y_2O_3 prior to $Y_2Ti_2O_7$. It also helps us to understand why titanium oxides grow much faster and can be found in the often-documented size range between 50 and 200 nm in diameter. Only titanium atoms, which are near yttrium, tend to diffuse towards the newly sequestered yttrium-rich precipitates to form the highly stable $Y_2Ti_2O_7$ phase in areas where enough oxygen is present. In addition, a low surface energy between $Y_2Ti_2O_7$ and the austenitic phase and the orientation relationship can be attributed to a much smaller size of the yttrium-rich oxides compared to the titanium-rich oxides.

Figure 5 shows the APT results after annealing had been performed at 700 °C and 1100 °C for 2 h each. It has to be noted, that huge carbides were found in both microstructures and that the displayed APT needles are not representative of the whole microstructure in general, due to their limited sample volume. The focus of the investigation has been on the growth of the oxide nano-particles and the elements which have been involved.

For both of the temperatures investigated, the nano-precipitates consist mainly of V, O, Cr, Ti, and Y and show a heterogeneous distribution inside the APT needles. Aluminum was also found in bigger Al_2O_3 precipitates with a diameter in the range of 30 to 80 nm. It is an impurity introduced during the steel production process and can often be found in mechanically alloyed steels [51, 52]. The analysis of the 700 °C APT needle confirms that nano-precipitates even exist inside big carbon precipitates and with that it can be inferred that the nano-precipitates were not able to hinder the growth of the carbides. The elements which sequestered carbon are V, Cr, Mn and W. All of these findings are in good agreement with the TEM results in Figure 4. However, the TEM results indicate that Y, Ti, and V are the major elements forming oxides, while APT results point to the fact that chromium also plays a role in the formation of the nano-precipitates. The results presented are also in good agreement with the Ellingham-Richardson diagrams, which show that the most likely elements to form oxides are yttrium, titanium, vanadium, manganese and chromium, in descending order [53–55].

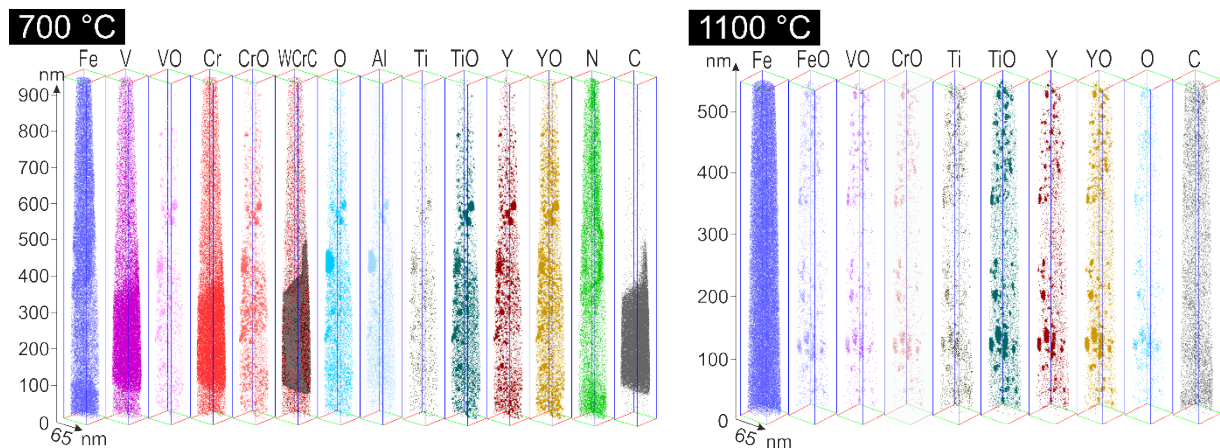


Figure 5 Particle distribution after a heat treatment of 700 °C (left) and 1100 °C (right) was applied for two hours.

Recently published research has demonstrated the stability of nano-precipitates and of the grain size during long-term heat treatments up to 1150 °C [12, 56]. No significant growth of precipitates was detected after their formation during extrusion. In the present study, the average radii of the yttrium and titanium-rich clusters were calculated by using the spherical equivalent radius (SER) R given by [57, 58]:

$$R = \sqrt{\frac{3N}{4\pi\rho Q}}$$

where N is the number of titanium and yttrium atoms in each precipitate, ρ is the density of the precipitates, and Q is the detection efficiency of the atom probe used, which was taken to be 0.4. For comparison reasons, the

calculated radii of precipitates were also determined by applying an often-used method: the Guinier radius R_g . It is given by [59]:

$$R_g = \sqrt{\frac{5}{3}} l_g,$$

where l_g is the radius of gyration. The measurements of the diameter were performed parallel to the analysis direction, as proposed in the publication by London et. al. [60]. The median of the size distribution of precipitates is shown in the box plot of Figure 6. Table 3 summarizes the APT results including the volume fraction of the precipitates f and their number density N . Four to six APT needles were tested for each condition, to give better statistics on the size of the precipitates.

Across all tested annealing temperatures, the mean diameter, determined using the Guinier radius, are larger than the values measured by the SER method at the same temperature. Nevertheless, both methods reveal the same trend shown in Figure 6: the median of the precipitate size distribution increases during an annealing, while the spread remains similar. An increasing median and mean diameter as well as a shift of the first and third quartile towards larger diameter prove that finding. The median is smaller than the mean value for every condition, which indicates a positive skewness of all three size distributions. The absolute values are less important than the fact that a change in diameter is visible even after short annealing times of only 2 hours. However, from a histogram plot (not shown) it can be seen, that the fraction of small precipitates between 1 and 3 nm decreases in favor of an increased fraction of precipitates in a range between 6 and 15 nm in diameter during annealing. Due to the high count of atoms for each condition, the standard deviation of the measured mean radius contains valuable information about the spread of the size distribution. The spread is also shown by the whiskers in Figure 6. They represent the minimum and maximum value of the measured diameter inside the one and a half times range of the interquartile range (IQR) [61].

In Table 3 a drop in the volume fraction is visible for the 1100 °C sample. Although four needles were tested at that temperature, due to the small sample volume and an inhomogeneous distribution of particles (see Figure 5), the volume fraction and the number density are locally dependent parameters. Because the same amount of yttrium and titanium was available in the material at all temperatures (which constitutes a constant volume fraction), the lower volume fraction can only be explained by the small investigated volume and an inhomogeneous particle distribution. The latter would cause a higher standard deviation of the volume fraction at 1100 °C, which was not detected. For that reason, areas with a lower volume fraction of particles must have been measured. Nevertheless, a general trend of declining values of number density of precipitates was observed at high temperatures, which clearly indicates that diffusion-controlled growth of precipitates occurred.

Carbon forms huge carbides with V, Cr, and W at high temperatures, due to its high diffusivity. It is not directly related nor dependent on the vacancy diffusion mechanism, but it diffuses to energetically favorable positions like dislocations or grain boundaries and can easily form carbides with the aforementioned elements [62].

It is still unclear why the ODS precipitates tend to grow after a short term annealing was conducted. An indirect effect of carbon on the growth of precipitates is suggested, which would explain the growth of precipitates as an accompanying process in the diffusion of carbon and the formation of carbides:

The diffusion of contributing elements in the carbide formation process facilitates the growth of titanium oxides and yttrium oxides. As the chemical composition changes, the diffusion coefficient of carbon in steel and the diffusion coefficient of other elements is affected in the same way by a change of the matrix material [63]. Carbon diffuses towards energetically beneficial positions and with that, changes the energy threshold for diffusion of other elements in the vicinity of carbon during its motion and, also, after the formation of the huge carbides. The diffusivity of titanium, oxygen and yttrium depends on a chemical gradient, the diffusion of other elements, the number of vacancies and the temperature.

For these reasons, we suggest that the existence and diffusion of carbon assists the diffusion of Cr, V, and W to form the aforementioned carbide phases. Several studies have proved that the alloying elements impact on the diffusion coefficient of carbon in steel [63, 64]. In an addition to this, we suggest there is an interdependence of carbon diffusion and the diffusion of other alloying elements. This means that the diffusion of yttrium or titanium could also be facilitated by the presence of carbon and it would explain the unexpected growth of precipitates.

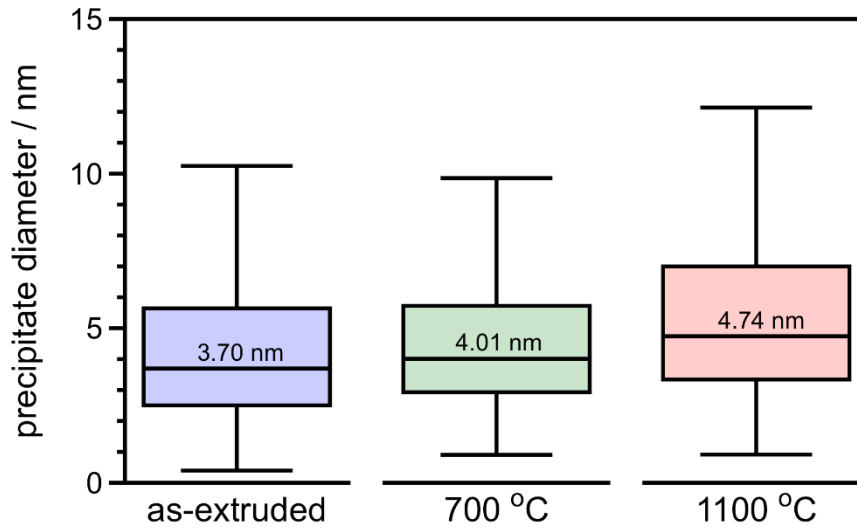


Figure 6 Box plot of the mean particle diameter before and after annealing determined using the Guinier radius. The median is illustrated by the line inside the box limiting the first and third quartile. The whiskers represent the minimum and maximum value inside the $1.5 \times \text{IQR}$. Outliers are not shown in this diagram.

Table 3 Results of the APT analysis of Y/Ti/O precipitates after a heat treatment of 2 hours. Mean diameter of precipitates d_{ODS} has been determined using the Guinier and the spherical equivalent radius (SER) method. The upper and lower limits represent the calculated standard deviation. f = volume fraction of precipitates; N = number density of precipitates.

Temperature / °C	No. of atoms / millions	Median / nm	Guinier: d_{ODS} / nm	SER: d_{ODS} / nm	f / %	N / $\times 10^{23} \text{m}^{-3}$	No. of particles
0	266	3.70	4.56 ± 3.28	2.83 ± 1.66	0.76 ± 0.39	3.03 ± 1.07	2106
700	373	4.01	5.18 ± 4.73	3.53 ± 2.20	0.76 ± 0.31	1.18 ± 0.48	1424
1100	290	4.74	5.88 ± 4.20	3.72 ± 2.16	0.43 ± 0.16	0.83 ± 0.63	428

3.3. Comparison of thermodynamic calculations and the microstructure

Figure 7A reveals the temperature-dependent phase composition of material PCA-2 in thermodynamic equilibrium when calculated using the software JMatPro 5.0, by Sente Software. The phase fraction of the M_{23}C_6 phase has a significant role in terms of the mechanical properties of the alloy and is marked with a red line in Figure 7. This diagram gives us an idea of the phase fraction of PCA-2 after heat treatments at 500, 700, 900 and 1100 °C. A phase fraction (wt.-%) of M_{23}C_6 of approximately 5.3 % at 500 and 700 °C, 4.5 % at 900 °C, and 1.5 % at 1100 °C would exist in the equilibrium state in the extruded PCA-2, under the assumption of an infinitely fast quenching process after the heat treatment. However, PCA-2 was only annealed for two hours and cannot be considered to be in an equilibrium condition. For a better understanding, the time dependency must be taken into account. The graph in Figure 7B shows the formation of the most important phases (with an arbitrarily chosen fraction of 0.5 %) with respect to the annealing time and temperature. A fraction of 0.5 % of M_{23}C_6 and M_7C_3 can already be obtained after 1 or 4 minutes at high temperatures of 1100 or 900 °C, respectively. The same amount of phase fraction can only be found after 300 minutes at temperatures of 700 °C. In Figure 7B, the applied annealing time of two hours is represented by a vertical black line, which also highlights that no phase fraction of a carbon-rich phase exceeds 0.5 % at temperatures below 730 °C for this annealing time. Further simulations have proved that the maximum phase fraction at 900 °C (4.5 %) and 1100 °C (1.5 %) was already reached within 46 or 5 minutes of annealing, respectively, but only around 0.2 % of the phase fraction of the M_{23}C_6 phase have been formed at 700 °C. Additionally, the M_7C_3 phase was found to be the carbide phase with the second highest phase fraction. Being a metastable phase, M_7C_3 transforms into the more stable M_{23}C_6 phase and is not shown in the phase diagram in the equilibrium state on the left-hand side of Figure 7 [33, 55]. However, time-dependent phase diagrams like Figure 7B can be inaccurate and the above mentioned times should only be considered as trends. For that reason, Figure 7A is the more reliable source of information in terms of the phase fractions of the annealed samples.

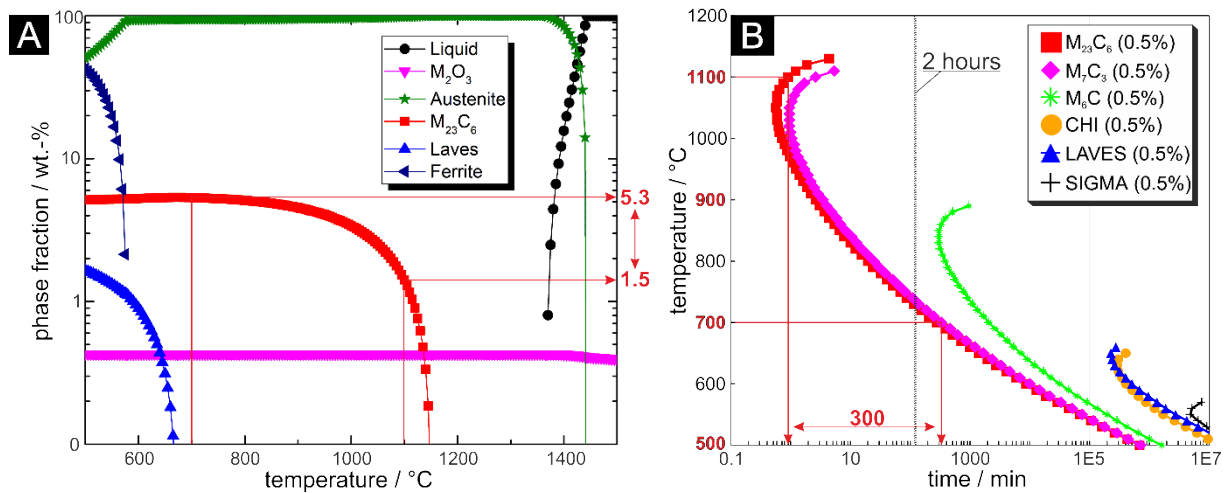


Figure 7 Thermodynamic simulation performed with JMatPro 5.0 using the chemical composition of PCA-2; A) the thermodynamic equilibrium of the phases as a function of the temperature and B) the temperature needed to form 0.5 wt.-% of the displayed precipitates/ intermetallic phases as a function of the holding time.

A comparison of the calculated results with the obtained microstructure (shown in Figure 8 and Figure 11), allows, us to draw conclusions about the impact of carbon, heat treatment and precipitates on the grain size. Figure 8 shows EBSD phase maps before and after different heat treatments. The normal direction of the maps is parallel to the extrusion direction. All maps were evaluated in the extrusion direction (ED). According to the information about the time-dependent formation of the carbide phases, gained from Figure 7, three phases were of special interest: the austenitic, the $M_{23}C_6$, and the M_7C_3 phase. These are displayed in red, green and teal in Figure 8, respectively. The grain boundaries are colored in black. Some areas have not shown Kikuchi patterns due to the surface roughness, which was generated by selective etching. These dark areas have been investigated using SEM energy dispersive x-ray (EDS) methods and were determined to be rich in titanium and oxygen. The different sizes of the two mentioned carbide phases are in good agreement with the calculated results shown in Figure 7, which indicate that more $M_{23}C_6$ is created in the investigated temperature range (image A) and that $M_{23}C_6$ precipitates are formed faster than the competing M_7C_3 precipitates (image B). The created $M_{23}C_6$ precipitates grow faster and are larger than the M_7C_3 precipitates and thus can be found as large particles. Precipitates of the M_7C_3 phase are visible along grain boundaries and were found to be smaller and more frequent.

The austenite grains of the as-extruded and the 500 °C sample are similar and exhibit some large grains. In between the austenitic matrix material, carbides with a diameter in the range 50 to 800 nm were found. Larger $M_{23}C_6$ precipitates had been formed (green), whereas the M_7C_3 phase (teal) was found to be sequestered in smaller precipitates along the grain boundaries of the austenitic matrix. Comparison of the as-extruded and the annealed condition reveals that the $M_{23}C_6$ precipitates increased in size after an annealing up to 900 °C. The 1100 °C sample, however, has larger titanium oxides and less carbides, which is also in good agreement with the thermodynamic simulations shown in Figure 7, due to the lower total limit of the carbide phase fraction (1.5 wt.-%).

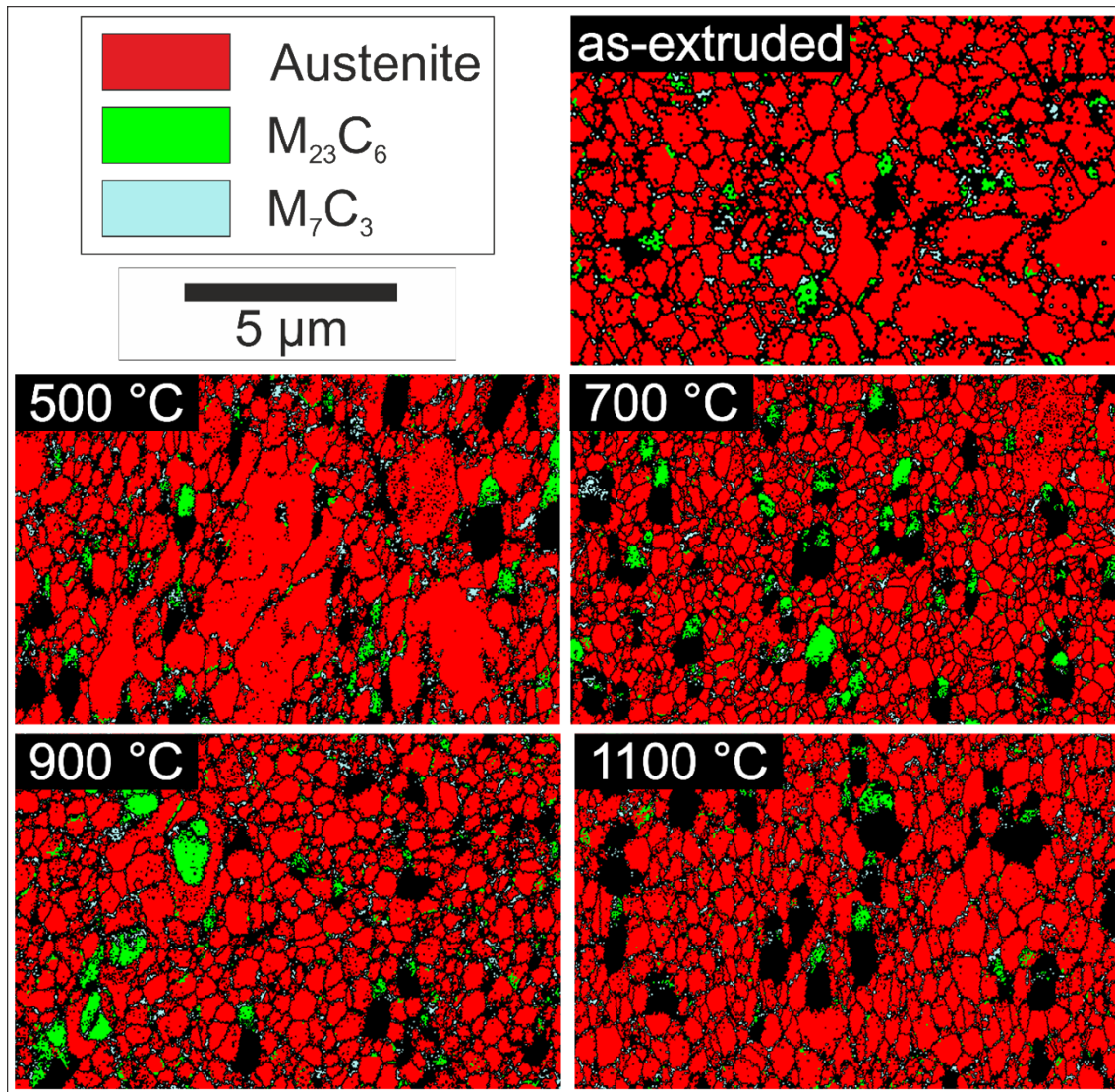


Figure 8 EBSD phase maps of austenite, $M_{23}C_6$ and M_7C_3 for all sample conditions.

A total of 13 area-% are found to belong to carbide phases in the as-extruded condition. 'Not-indexed' areas have not been taken into account for the calculation of the area fraction, which leads to an increased value for all other phases in general. Only the trend of the area fractions (not the total values) were evaluated for comparison reasons. The area fraction of the two most prominent phases besides the austenitic phase (the $M_{23}C_6$ and the M_7C_3 phase) are depicted in Figure 9, together with the sum of these carbides. An increased aggregate of carbides (which was higher than the average (13 area-%)) was found after an annealing at 900 °C. At all other temperatures the total area fraction of carbides remains similar. Nevertheless, the ratio between the two carbide phases changes. The phase fraction of $M_{23}C_6$ rises steadily for increased annealing temperatures until a peak at 900 °C was reached. A drop of the maximum area fraction, from around 7.5 area-% to 5 area-%, was observed for an increased annealing temperature of 1100 °C. This decline is linked to the lower maximum of carbides at this temperature of only 1.5 wt.-%, according to Figure 7. A trend for the M_7C_3 could not be observed however, Figure 8 shows a decreased grain size after an annealing at temperatures of 700 °C and above. A smaller grain size is tantamount to more grain boundaries, which are the sites where M_7C_3 carbides were found. More grain boundaries also provide more diffusion paths and formation sites for carbon and carbides, which decreases their size and also their detectability. This could be a possible explanation for the drop of the area fraction after an annealing at 700 °C was carried out. This investigation of the carbides highlights that the amount of both carbide phases can be correlated with each other and is directly linked to the chosen annealing temperature.

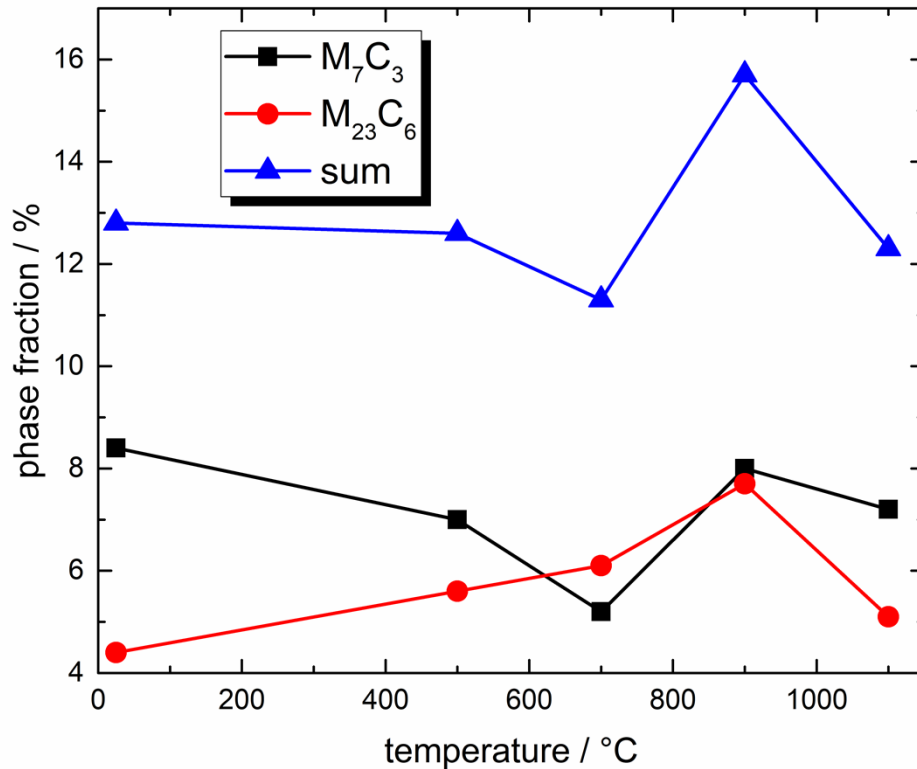


Figure 9 Area fraction of the analyzed carbide phases and their sum for all investigated temperatures.

After the carbide formation was investigated, the texture and the grain size were examined and summarized in Figure 10 and Figure 11. Inverse pole figure (IPF) maps and grain average misorientation (GAM) maps of as-extruded and annealed material are shown in Figure 10. In the as-extruded sample, most grains have a (001) orientation, which is typical for extruded material and, in this material, was found to be 7.8 times more likely than a random orientation. Approximately 5 % of the grains exhibit a (001)<010> orientation, which is linked to an occurrence of dynamic recrystallization [12, 23]. The samples annealed at 500, 700 and 900 °C have some larger grains with a (111) orientation (not displayed). In terms of the grain size, a change towards a smaller grain size can be observed for higher annealing temperatures. This phenomenon can be explained by comparing the GAM of as-extruded and annealed material on the bottom of Figure 10. The GAM is able to give information about the misorientation within a single grain and, with that, an indication of the driving force that lead to recrystallization. Small angle grain boundaries and a high dislocation density contribute to the average misorientation. During an annealing treatment, recrystallization occurs in those areas and small grains form and grow until they get pinned by precipitates. These newly-formed grains have a much lower average misorientation and can be seen on the bottom right-hand side in Figure 10.

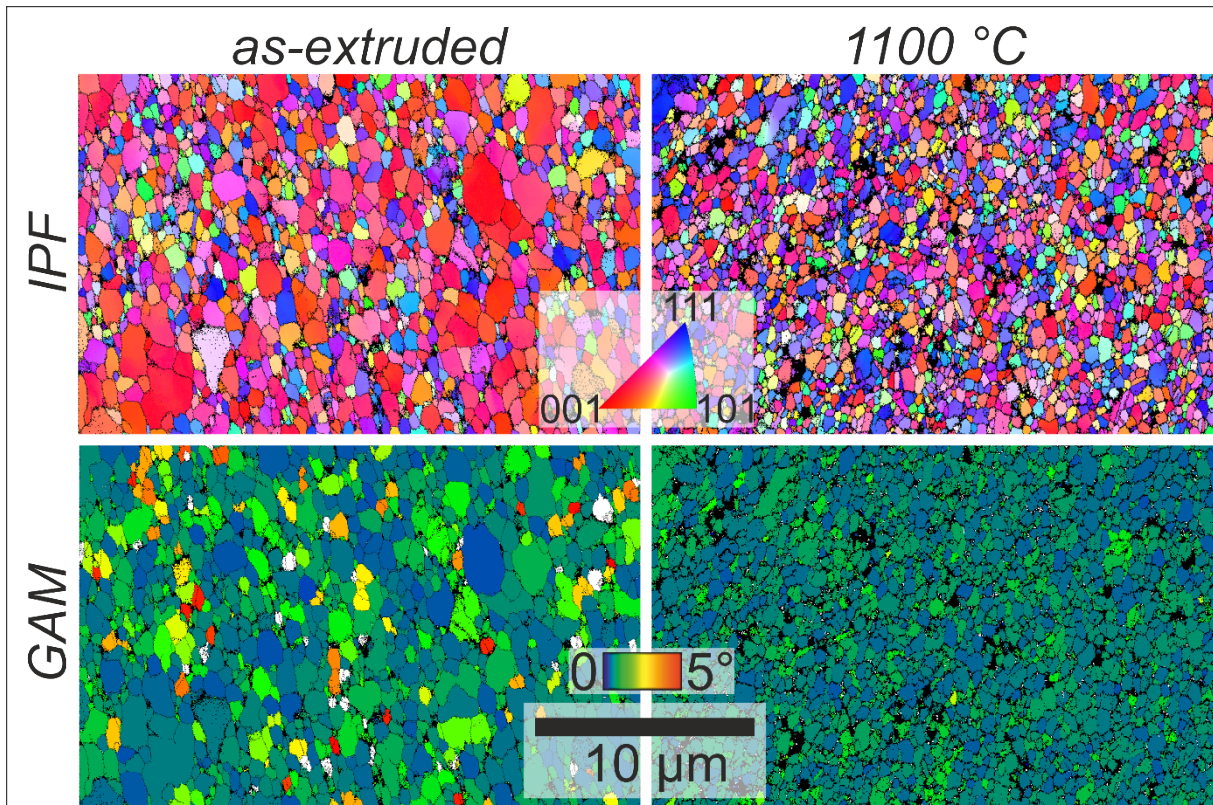


Figure 10 Inverse pole figure and grain average misorientation maps before and after annealing at 1100 °C.

In Figure 11, the austenitic grain size dependence on the annealing temperature is evaluated using two methods: a number and an area averaging. The first method is the conventional numerical average, while the second method comprises weighting the average value by the area of each grain. If the grain size is uniform, both methods should generate average grain size values which are close to each other. Therefore, plotting both graphs and comparing the difference between them gives information about the homogeneity of the grain size. It is often reported that ODS steel tends to form a bimodal grain size [32, 65, 66]. In the austenitic grain size dependence on the annealing temperature is evaluated using two methods: a number and an area averaging. The first mentioned is the conventional numerical average, while the last mentioned method is weighing the value of the average by the area of each grain. If the grain size is uniform, both methods should generate average grain size values, which are close to each other. Therefore, plotting both graphs and comparing the difference between them gives information about the homogeneity of the grain size. It is often reported, that ODS steel tend to form a bimodal grain size [32, 65, 66].

In Figure 11, it can be seen that in the as-extruded condition and after an annealing at 500 °C the grain size is considered to be bimodal, showing differences in the average grain size between both evaluation methods of between 0.7 and 0.9 µm. The standard deviation of both calculated grain size averages gives additional information about the grain size distribution. Its decrease, in addition to the smaller gap between the determined values of the grain size at annealing temperatures of 700 °C and above, indicates that the microstructure becomes more homogenous at higher annealing temperatures. No relationship between the resulting microstructure (shown in Figure 10) and the carbide formation and evaluation (shown in Figure 8 and Figure 9) was found and, therefore, a long-term annealing of a carbon-rich austenitic ODS steel is necessary to investigate the growth and change of precipitates and grains to reveal the full impact of carbon on the microstructure and mechanical properties. Development of the grain size of an austenitic ODS steel after annealing has been reported elsewhere and seems to be dominated by polygonisation and a subsequent transformation from sub-grain to high-angle grain boundaries [12, 67]. The transformation takes place by grain rotation, which happens when the recrystallization process is initialized [68, 69]. The small size of the newly formed grains is than stabilized by a process known as Zener-pinning [56, 70–72]. Thereby, the precipitates hinder grain boundary migration and the small grain size remains until the driving force for further grain growth is high enough to

overcome the pinning pressure. The driving force is governed by several factors, including diffusion and chemical gradients. These two factors are severely influenced by carbon and need to be investigated in future research.

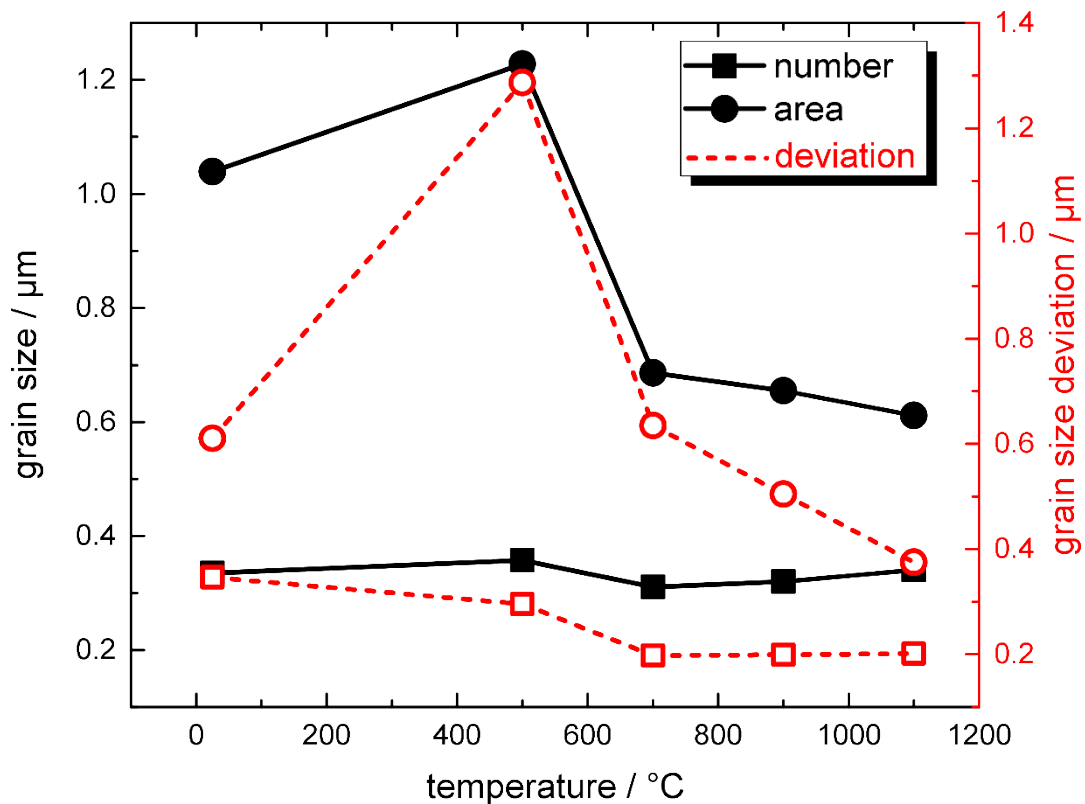


Figure 11 Change of the grain size after an annealing of 2 hours at different temperatures averaged by number (numerical) and by area of each grain. The standard deviation of the grain size is displayed in red and is linked to the right axis.

4. Conclusions

A comprehensive study on extruded austenitic ODS steel has been carried out to reveal the influence of carbon on precipitates and grain size, before and after annealing at 4 different temperatures between 500 and 1100 °C. In comparison with recently published results it was possible to summarize the findings of this study as follows:

- No direct impacts of carbon on the orientation relationship or the precipitates were detectable.
- The orientation relationship between precipitates and matrix for austenitic ODS steels is dependent on the size of the precipitates and was found to be in good agreement with the results of other researchers.
- A surprising growth of precipitates is observed, even for a short annealing time of only 2 h. A long-term annealing needs to be performed to investigate the evolution of the microstructure thoroughly.
- Cr-W-Ti-C precipitates have been found in the as-extruded material and under all annealing conditions. According to thermodynamic simulations, these precipitates are $M_{23}C_6$ or M_7C_3 phase. The volume fraction and the size of these carbides strongly depend on the applied heat treatment temperature. $M_{23}C_6$ forms large precipitates with a size up to 1 μm in diameter, while M_7C_3 can only be found in smaller precipitates along the grain boundaries.
- An indirect effect of carbon on the growth of Y-Ti-O-rich clusters is suggested, which would explain the growth of these particles as a process that accompanies the diffusion of carbon and the formation of

carbides. The diffusion of contributing elements in the carbide formation process, facilitates the growth of titanium oxides and yttrium oxides.

- A heat-treatment greater than 700 °C leads to a decreased inhomogeneity in grain size, which can be explained by inhibited grain growth during static recrystallization caused by Zener drag.
- The grain size decreases during annealing after only a short time, which can be explained by recrystallization and the pinning of the newly formed grain boundaries. The thermally activated formation of high angle grain boundaries (after recovery), results in a lower average grain misorientation, followed by a suppression of grain growth due to the pinning pressure exerted by the precipitates.

Acknowledgements

This work has been carried out within the framework of the German Helmholtz Association and has received funding under the topic “Materials Research for the Future Energy Supply”.

This work was partly carried out with the support of the Karlsruhe Nano Micro Facility (KNMF), a Helmholtz Research Infrastructure at Karlsruhe Institute of Technology (KIT).

I acknowledge the work of Rainer Ziegler (KIT), who helped with the production of the studied alloy. Thanks are also due to Chad Parish (ORNL), who helped with the TEM images. Thanks to the team of Dr. Bergfeldt, who carried out the chemical analysis of the extruded material.

Atom probe tomography research was conducted at the Center for Nanophase Materials Sciences, which is a DOE Office of Science User Facility.

References

1. Zhao Q, Yu L, Liu Y, et al (2017) Microstructure and tensile properties of a 14Cr ODS ferritic steel. *Mater Sci Eng A* 680:347–350 . doi: 10.1016/j.msea.2016.10.118
2. Tanigawa H, Gaganidze E, Hirose T, et al (2017) Development of benchmark reduced activation ferritic / martensitic steels for fusion energy applications. *Nucl Fusion* 57:92004 . doi: 10.1088/1741-4326/57/9/092004
3. Raman L, Gothandapani K, Murty BS (2016) Austenitic oxide dispersion strengthened steels: A review. *Def Sci J* 66:316–322 . doi: 10.14429/dsj.66.10205
4. Kim TK, Bae CS, Kim D, et al (2008) Microstructural Observation and Tensile Isotropy of an Austenitic ODS Steel. *Nucl Eng Technol* 40:305
5. Phaniraj MP, Kim D-II, Shim J-HH, Cho YW (2009) Microstructure development in mechanically alloyed yttria dispersed austenitic steels. *Acta Mater* 57:1856–1864 . doi: 10.1016/j.actamat.2008.12.026
6. Wang M, Zhou Z, Sun H, et al (2013) Microstructural observation and tensile properties of ODS-304 austenitic steel. *Mater Sci Eng A* 559:287–292 . doi: 10.1016/j.msea.2012.08.099
7. Miao Y, Mo K, Zhou Z, et al (2015) On the microstructure and strengthening mechanism in oxide dispersion-strengthened 316 steel: A coordinated electron microscopy, atom probe tomography and in situ synchrotron tensile investigation. *Mater Sci Eng A* 639:585–596 . doi: 10.1016/j.msea.2015.05.064
8. Xu Y, Zhou Z, Li M, He P (2011) Fabrication and characterization of ODS austenitic steels. *J Nucl Mater* 417:283–285 . doi: 10.1016/j.jnucmat.2010.12.155

9. Lu Q, Xu W, van der Zwaag S (2013) Computational design of precipitation strengthened austenitic heat-resistant steels. *Philos Mag* 93:3391–3412 . doi: 10.1080/14786435.2013.809493
10. Suresh K, Nagini M, Vijay R, et al (2016) Microstructural studies of oxide dispersion strengthened austenitic steels. *Mater Des* 110:519–525 . doi: 10.1016/j.matdes.2016.08.020
11. Wang M, Zhou Z, Sun H, et al (2012) Effects of plastic deformations on microstructure and mechanical properties of ODS-310 austenitic steel. *J Nucl Mater* 430:259–263 . doi: 10.1016/j.jnucmat.2012.07.014
12. Gräning T, Rieth M, Hoffmann J, Möslang A (2017) Production, microstructure and mechanical properties of two different austenitic ODS steels. *J Nucl Mater* 487:348–361 . doi: 10.1016/j.jnucmat.2017.02.034
13. Suryanarayana C (2011) Synthesis of nanocomposites by mechanical alloying. *J Alloys Compd* 509:S229–S234 . doi: 10.1016/j.jallcom.2010.09.063
14. P. S. Gilman JSB (1999) Mechanical alloying. *Met Powder Rep* 54:38 . doi: 10.1016/S0026-0657(00)86280-3
15. Gräning T, Rieth M, Möslang A, et al (2018) Investigation of precipitate in an austenitic ODS steel containing a carbon-rich process control agent. *Nucl Mater Energy* accepted
16. Schindelin J, Rueden CT, Hiner MC, Eliceiri KW The ImageJ ecosystem: An open platform for biomedical image analysis. *Mol Reprod Dev* 82:518–29 . doi: 10.1002/mrd.22489
17. Mumme WG, Wadsley AD (1968) The structure of orthorhombic Y_2TiO_5 , an example of mixed seven- and fivefold coordination. *Acta Crystallogr Sect B Struct Crystallogr Cryst Chem* 24:1327–1333 . doi: 10.1107/S0567740868004243
18. Haile SM, Wuensch BJ, Prince E (1989) Neutron Rietveld Analysis of Anion and Cation Disorder in the Fast-Ion Conducting Pyrochlore System $Y_2(ZrTi_{1-x})_2O_7$. *MRS Proc* 166:81 . doi: 10.1557/PROC-166-81
19. Coduri M, Scavini M, Allieta M, et al (2013) Defect Structure of Y-Doped Ceria on Different Length Scales. *Chem Mater* 25:4278–4289 . doi: 10.1021/cm402359d
20. Miller MK, Kenik EA, Russell KF, et al (2003) Atom probe tomography of nanoscale particles in ODS ferritic alloys. *Mater Sci Eng A* 353:140–145 . doi: 10.1016/S0921-5093(02)00680-9
21. Saber M, Xu W, Li L, et al (2014) Size effect of primary Y_2O_3 additions on the characteristics of the nanostructured ferritic ODS alloys: Comparing as-milled and as-milled/annealed alloys using S/TEM. *J Nucl Mater* 452:223–229 . doi: 10.1016/j.jnucmat.2014.05.014
22. Seol J-B, Na S-H, Gault B, et al (2017) Core-shell nanoparticle arrays double the strength of steel. *Sci Rep* 7:42547 . doi: 10.1038/srep42547
23. Raabe D (2014) Recovery and Recrystallization: Phenomena, Physics, Models, Simulation. In: *Physical Metallurgy*. Elsevier B.V., pp 2291–2397
24. Ribis J, Lescoat ML, Zhong SY, et al (2013) Influence of the low interfacial density energy on the coarsening resistivity of the nano-oxide particles in Ti-added ODS material. *J Nucl Mater* 442: . doi: 10.1016/j.jnucmat.2012.10.051
25. Ribis J, De Carlan Y (2012) Interfacial strained structure and orientation relationships of the nanosized oxide particles deduced

- from elasticity-driven morphology in oxide dispersion strengthened materials. *Acta Mater* 60:238–252 . doi: 10.1016/j.actamat.2011.09.042
26. Boulnat X, Perez M, Fabrègue D, et al (2016) Characterization and modeling of oxides precipitation in ferritic steels during fast non-isothermal consolidation. *Acta Mater* 107:390–403 . doi: 10.1016/j.actamat.2016.01.034
 27. Miao Y, Mo K, Cui B, et al (2015) The interfacial orientation relationship of oxide nanoparticles in a hafnium-containing oxide dispersion-strengthened austenitic stainless steel. *Mater Charact* 101:136–143 . doi: 10.1016/j.matchar.2015.01.015
 28. Humphreys FJ, Hatherly M (1996) Recrystallization and related annealing phenomena, Repr. with. Pergamon, Oxford [u.a.]
 29. Hirsch PB, Humphreys FJ (1969) Plastic deformation of two-phase alloys containing small non-deformable particles. *Phys Strength Plast* 189–216
 30. Briant CL (1983) Embrittlement of engineering alloys. Acad. Pr., New York [u.a.]
 31. Giang NA, Kuna M, Hütter G (2017) Influence of carbide particles on crack initiation and propagation with competing ductile-brittle transition in ferritic steel. *Theor Appl Fract Mech* 92:89–98 . doi: 10.1016/j.tafmec.2017.05.015
 32. Brandes MC, Kovarik L, Miller MK, Mills MJ (2012) Morphology, structure, and chemistry of nanoclusters in a mechanically alloyed nanostructured ferritic steel. *J Mater Sci* 47:3913–3923 . doi: 10.1007/s10853-012-6249-x
 33. Small M, Ryba E (1981) Calculation and evaluation of the gibbs energies of formation of Cr₃C₂, Cr₇C₃, and Cr₂₃C₆. *Metall Trans A* 12:1389–1396 . doi: 10.1007/BF02643683
 34. London AJ, Lozano-Perez S, Santra S, et al (2014) Comparison of atom probe tomography and transmission electron microscopy analysis of oxide dispersion strengthened steels. *J Phys Conf Ser* 522:12028 . doi: 10.1088/1742-6596/522/1/012028
 35. Song M, Sun C, Jang J, et al (2013) Microstructure refinement and strengthening mechanisms of a 12Cr ODS steel processed by equal channel angular extrusion. *J Alloys Compd* 577:247–256 . doi: 10.1016/j.jallcom.2013.04.198
 36. Parish CM, Field KG, Certain AG, Wharry JP (2015) Application of STEM characterization for investigating radiation effects in BCC Fe-based alloys. *J Mater Res* 30:1275–1289 . doi: 10.1557/jmr.2015.32
 37. Sakasegawa H, Legendre F, Boulanger L, et al (2011) Stability of non-stoichiometric clusters in the MA957 ODS ferritic alloy. *J Nucl Mater* 417:229–232 . doi: 10.1016/j.jnucmat.2010.12.056
 38. Williams CA, Unifantowicz P, Baluc N, et al (2013) The formation and evolution of oxide particles in oxide-dispersion-strengthened ferritic steels during processing. *Acta Mater* 61:2219–2235 . doi: 10.1016/j.actamat.2012.12.042
 39. Bruemmer S., Charlot L. (1986) Development of grain boundary chromium depletion in type 304 and 316 stainless steels. *Scr Metall* 20:1019–1024 . doi: 10.1016/0036-9748(86)90428-X
 40. Yang Y, Field KG, Allen TR, Busby JT (2016) Roles of vacancy/interstitial diffusion and segregation in the microchemistry at grain boundaries of irradiated Fe-Cr-Ni alloys. *J Nucl Mater* 473:35–53 . doi: 10.1016/j.jnucmat.2016.02.007
 41. Klimenkov M, Lindau R, Möslang A (2010) Transmission electron microscopy study of Ar-filled bubbles in steel. *J Microsc* 237:497–500 . doi: 10.1111/j.1365-2818.2009.03307.x

42. Klimenkov M (2011) Quantitative measurement of argon inside of nano-sized bubbles in ODS steels. *J Nucl Mater* 411:160–162 . doi: 10.1016/j.jnucmat.2011.01.104
43. Yang L, Jiang Y, Wu Y, et al (2016) The ferrite/oxide interface and helium management in nano-structured ferritic alloys from the first principles. *Acta Mater* 103:474–482 . doi: 10.1016/j.actamat.2015.10.031
44. Edmondson PD, Parish CM, Li Q, Miller MK (2014) Thermal stability of nanoscale helium bubbles in a 14YWT nanostructured ferritic alloy. *J Nucl Mater* 445:84–90 . doi: 10.1016/j.jnucmat.2013.10.024
45. Parish CM, Miller MK (2014) Aberration-Corrected X-Ray Spectrum Imaging and Fresnel Contrast to Differentiate Nanoclusters and Cavities in Helium-Irradiated Alloy 14YWT. *Microsc Microanal* 20:613–626 . doi: 10.1017/S1431927614000312
46. Klimiankou M, Lindau R, Möslang A (2004) TEM characterization of structure and composition of nanosized ODS particles in reduced activation ferritic-martensitic steels. *J Nucl Mater* 329–333:347–351 . doi: 10.1016/j.jnucmat.2004.04.083
47. Odette GR, Alinger MJ, Wirth BD (2008) Recent Developments in Irradiation-Resistant Steels. *Annu Rev Mater Res* 38:471–503 . doi: 10.1146/annurev.matsci.38.060407.130315
48. Wu Y, Haney EM, Cunningham NJ, Odette GR (2012) Transmission electron microscopy characterization of the nanostructures in nanostructured ferritic alloy MA957. *Acta Mater* 60:3456–3468 . doi: 10.1016/j.actamat.2012.03.012
49. Hilger I, Tegel M, Gorley MJ, et al (2014) The structural changes of Y₂O₃ in ferritic ODS alloys during milling. *J Nucl Mater* 447:242–247 . doi: 10.1016/j.jnucmat.2014.01.026
50. Okita T, Wolfer WG, Garner F a., Sekimura N (2005) Effects of titanium additions to austenitic ternary alloys on microstructural evolution and void swelling. *Philos Mag* 85:2033–2048 . doi: 10.1080/14786430412331331871
51. Miao Y, Mo K, Zhou Z, et al (2015) In situ synchrotron tensile investigations on the phase responses within an oxide dispersion-strengthened (ODS) 304 steel. *Mater Sci Eng A* 625:146–152 . doi: 10.1016/j.msea.2014.12.017
52. Miao Y (2015) Advanced Characterizations of Austenitic Oxide Dispersion-Strengthened (Ods) Steels for High-Temperature Reactor Applications. University of Illinois at Urbana-Champaign
53. Robino CV (1996) Representation of mixed reactive gases on free energy (Ellingham-Richardson) diagrams. *Metall Mater Trans B* 27:693–693 . doi: 10.1007/BF02915669
54. Ellingham HJT (1944) Reductibility of oxides and sulphides in metallurgical processes. *J Soc Chem Ind* 63:125–160 . doi: 10.1002/jctb.5000630201
55. Shatynski SR (1979) The thermochemistry of transition metal carbides. *Oxid Met* 13:105–118 . doi: 10.1007/BF00611975
56. Mao X, Oh KH, Jang J (2016) Evolution of ultrafine grained microstructure and nano-sized semi-coherent oxide particles in austenitic oxide dispersion strengthened steel. *Mater Charact* 117:91–98 . doi: 10.1016/j.matchar.2016.04.022
57. Kolli RP, Seidman DN (2007) Comparison of Compositional and Morphological Atom-Probe Tomography Analyses for a Multicomponent Fe-Cu Steel. *Microsc Microanal* 13:272–284 . doi: 10.1017/S1431927607070675
58. Bachhav M, Robert Odette G, Marquis EA (2014) α' precipitation in neutron-irradiated Fe-Cr alloys. *Scr Mater* 74:48–51 . doi: 10.1016/j.scriptamat.2013.10.001

59. Miller MK (2004) Atom Probe Tomography and the Local Electrode Atom Probe. *Microsc Microanal* 10:150–151 . doi: 10.1017/S1431927604881157
60. London AJ, Lozano-Perez S, Moody MP, et al (2015) Quantification of oxide particle composition in model oxide dispersion strengthened steel alloys. *Ultramicroscopy* 159:360–367 . doi: 10.1016/j.ultramic.2015.02.013
61. Krzywinski M, Altman N (2014) Visualizing samples with box plots. *Nat Methods* 11:119–120 . doi: 10.1038/nmeth.2813
62. Veiga RGA, Perez M, Becquart CS, et al (2010) Effect of the stress field of an edge dislocation on carbon diffusion in α -iron: Coupling molecular statics and atomistic kinetic Monte Carlo. *Phys Rev B - Condens Matter Mater Phys* 82:1–11 . doi: 10.1103/PhysRevB.82.054103
63. Gegner J, Vasilyev AA, Wilbrandt P, Kaffenberger M (2012) Alloy Dependence of the Diffusion Coefficient of Carbon in Austenite and Analysis of Carburization Profiles in Case Hardening of Steels. *Proc Int Conf Mater Technol Model* 2012 261–287 . doi: 10.13140/2.1.3871.2646
64. Lee S-J, Matlock DK, Van Tyne CJ (2011) An Empirical Model for Carbon Diffusion in Austenite Incorporating Alloying Element Effects. *ISIJ Int* 51:1903–1911 . doi: 10.2355/isijinternational.51.1903
65. Mao X, Kang SH, Kim TK, et al (2016) Microstructure and Mechanical Properties of Ultrafine-Grained Austenitic Oxide Dispersion Strengthened Steel. *Metall Mater Trans A* 47:5334–5343 . doi: 10.1007/s11661-016-3570-z
66. Chauhan A, Straßberger L, Führer U, et al (2017) Creep-fatigue interaction in a bimodal 12Cr-ODS steel. *Int J Fatigue* 102:92–111 . doi: 10.1016/j.ijfatigue.2017.05.003
67. Chen CL, Tatlock GJ, Jones AR (2009) Effect of annealing temperatures on the secondary re-crystallization of extruded PM2000 steel bar. *J Microsc* 233:474–481 . doi: 10.1111/j.1365-2818.2009.03134.x
68. Salahinejad E, Amini R, Hadianfard MJ (2012) Structural evolution during mechanical alloying of stainless steels under nitrogen. *Powder Technol* 215–216:247–253 . doi: 10.1016/j.powtec.2011.10.012
69. Suryanarayana C (2001) Mechanical alloying and milling. *Prog Mater Sci* 46:1–184 . doi: 10.1016/S0079-6425(99)00010-9
70. Nes E, Ryum N, Hunderi O (1985) On the Zener drag. *Acta Metall* 33:11–22 . doi: 10.1016/0001-6160(85)90214-7
71. Sandim HRZ, Renzetti RA, de Oliveira Zimmermann AJ, et al (2012) Annealing Behavior of Ferritic-Martensitic ODS-Eurofer Steel: Effect of Y_2O_3 Particles on Recrystallization. *Mater Sci Forum* 715–716:629–634 . doi: 10.4028/www.scientific.net/MSF.715-716.629
72. Miodownik MA (2006) Grain boundary engineering with particles. *Scr Mater* 54:993–997 . doi: 10.1016/j.scriptamat.2005.11.040